SCIENCE CHINA
Information Sciences

CrossMark click for updates

• LETTER •

April 2024, Vol. 67, Iss. 4, 149401:1–149401:2
https://doi.org/10.1007/s11432-023-3940-x

Improved RF power performance via electrostatic shielding effect using AlGaN/GaN/graded-AlGaN/GaN double-channel structure

Chunzhou SHI[1], Ling YANG[2*], Meng ZHANG[2], Hao LU[2], Mei WU[2], Bin HOU[2], Xuerui NIU[2], Qian YU[2], Wenliang LIU[2], Wenze GAO[2], Xiaohua MA[2] & Yue HAO[2]

[1] *School of Advanced Materials and Nanotechnology, Xidian University, Xi'an* 710071*, China;*
[2] *State Key Discipline Laboratory of Wide Bandgap Semiconductor Technology, Xidian University, Xi'an* 710071*, China*

Received 6 September 2023/Revised 28 November 2023/Accepted 19 January 2024/Published online 27 March 2024

GaN-based high-electric-mobility transistors (HEMTs) have been investigated thoroughly because of their promising applications in high-frequency, -voltage, and -power applications.

However, the theoretical material limit prevents conventional single-heterostructure GaN HEMTs from achieving high performance despite numerous efforts [1–3]. GaN-based double-channel HEMTs (DC-HEMTs) have attracted extensive attention due to their higher current drive than single channel HEMTs and the potential advantages of two channels in the RF circuit design. Nevertheless, traditional AlGaN/GaN/AlGaN/GaN DC-HEMTs suffer from poor off-state current and short-channel effect due to an extra AlGaN barrier between the two channels [4]. A thinner AlN barrier was used to minimize the thickness of double channels and to improve gate control for the bottom channel while maintaining the transistor's benefit of high current drive. However, AlN has a larger lattice mismatch with GaN than AlGaN with GaN and a larger inverse piezoelectric effect [5], resulting in the decreased total carrier density and worsened breakdown characteristics of the device. In addition, in terms of realizing high power, GaN HEMTs cannot neglect the lag phenomenon at high voltage. A DC-HEMT with a graded bottom channel (DCGC-HEMT) was proposed as a solution to rectify these issues. An $Al_{0.3}Ga_{0.7}N/GaN/Al_xGa_{1-x}N$ layer is the foundation of the DC structure, where x is graded top-down from 0.3 to 0, as shown in Figure 1(a). A reference DC-HEMT with an ultrathin bottom AlN barrier (3-nm AlN, DCTB-HEMT) is offered for ensuring the rigor of the entire work to methodically investigate the benefits of DCGC-HEMT, as shown in Figure 1(b).

Experiment. The DCGC-HEMT and DCTB-HEMT heterostructures were grown via metal-organic chemical vapor deposition (MOCVD) on 3-inch SiC substrates. The fabrication of devices consists of ohmic contact, isolation, surface passivation, and gate metal evaporation. Finally, both DCGC- and DCTB-HEMT were systematically investigated through TCAD (technology computer aided design) simulation, transmission electron microscopy, direct current measurement, drain lag test, and large signal test.

Results and discussion. The direct current measurement was performed to evaluate the saturation current and breakdown characteristics of the device. Figure 1(c) shows the transfer curves of the two devices. The saturated drain currents (gate voltage bias at 2 V) of DCGC- and DCTB-HEMT are 1298.8 and 1140.3 mA/mm, respectively. When the gate voltage (V_g) positively shifts, the bottom and upper channels subsequently turn on.

The maximum transconductance ($G_{m,max}$) of the bottom channel from DCTB-HEMT (209 mS/mm) is greater than that from DCGC-HEMT (189 mS/mm) due to the different gate-to-channel distance. The $G_{m,max}$ of the upper channel from the two devices is nearly the same (226.8 mS/mm from DCTB-HEMT and 221.7 mS/mm from DCGC-HEMT) due to the same structural upper heterostructure. Figure 1(d) shows the breakdown characteristics of DCTB- and DCGC-HEMT. The measurement was operated in an off-state at $V_{GS} = -10$ V, guaranteeing pinch-off for two devices. Evidently, the breakdown voltage is increased from 124 V of DCTB-HEMT to 165 V of DCGC-HEMT, i.e., 41 V increase.

Figure 1(e) shows the drain transient current ($I_{d.t}$) normalized to the final of DCTB/DCGC-HEMT at three temperatures, and the inset image Figure 1(f) shows the bias condition versus time. The current recovering process of DCTB-HEMT is considerably more rapid, which is caused by more electrons being captured by traps. Figures 1(g) and (h) show the related differential values of the transient current from the two devices at different temperatures, and DCGC-HEMT has a lower peak value at each temperature due to the good shielding effect on the traps. The activation energies from the two devices are 0.6307 and 0.6398 eV, implying the same trap.

The normalized I_D at $V_{DS} = 20/40$ V and drain lag ratio (DLR) of the two devices with different V_{DS} are shown in Figures 1(i) and (j), respectively. According to the Figures 1(i) and (j), the drain lag of both devices degrades with

* Corresponding author (email: yangling@xidian.edu.cn)

© Science China Press 2024

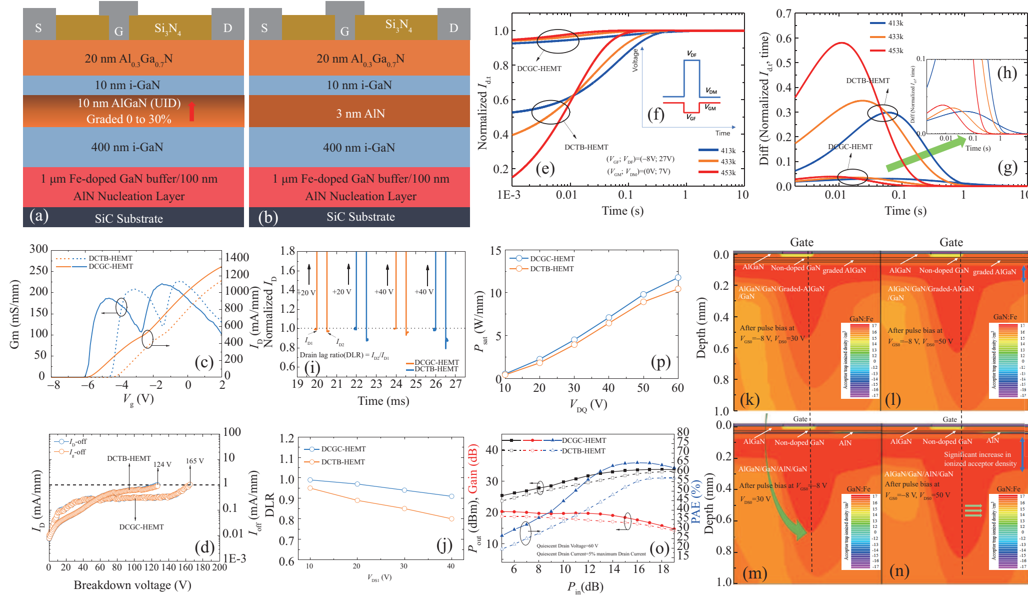

Figure 1 (Color online) Heterostructures of (a) DCGC- and (b) DCTB-HEMT, respectively. (c) Transfer curves and (d) breakdown voltages of DCGC- and DCTB-HEMT; (e) drain transient current normalized to its final value in DCGC- and DCTB-HEMT; (f) bias condition versus time; (g) time related differential value of transient current from DCGC- and DCTB-HEMT at different temperatures; (h) partial enlarged drawing of figure (g); (i), (j) normalized $I_{\rm D}$ at $V_{\rm DS} = 20/40$ V and DLR of the two devices for different $V_{\rm DS}$; (k) and (l)/(m) and (n) simulation of acceptor trap ionized density of DCGC-/DCTB-HEMT at $(V_{\rm g}, V_{\rm d}) = (-8, 30)$ V and $(V_{\rm g}, V_{\rm d}) = (-8, 50)$ V; (o) output performance of the two devices at $V_{\rm DQ} = 60$ V; (p) saturated output power ($P_{\rm sat}$) of DCGC-/DCTB-HEMT with different $V_{\rm DQ}$.

$V_{\rm DS}$. Moreover, the DLR characteristics of DCGC-HEMT are superior to those of DCTB-HEMT under the same drain bias condition. On the one hand, DLR is heavily influenced by the drain bias condition; on the other hand, two different bottom barriers show different suppressions in drain lag. Figures 1(k)–(n) are simulations of the acceptor trap ionized density of DCGC-/DCTB-HEMT under different bias conditions from TCAD. Considering the iron doping tail effect, the doping depth is set substantially close to the bottom channel. Evidently, with increasing $V_{\rm DS0}$, the acceptor trap ionized densities of both devices increase. Nevertheless, the total ionized trap density of DCGC-HEMT always remains less than that of DCTB-HEMT under the same bias condition, indicating that the bottom barrier of the two devices affects the activation of acceptor traps differently, resulting in their different acceptor trap ionized densities.

In the 3.6-GHz continuous-wave mode and class AB bias condition, the on-wafer measurement of DCGC-/DCTB-HEMTs was performed using a Murray load-pull system to analyze their large-signal characteristics. Figure 1(o) shows the output performance of the two devices at $V_{\rm DQ} = 60$ V. DCGC-HEMT has a maximum power additional efficiency ($\rm PAE_{max}$) of 64.98% and a saturated output power ($P_{\rm sat}$) of 11.76 W/mm, while DCTB has a $\rm PAE_{max}$ of 56.7% and a $P_{\rm sat}$ of 10.30 W/mm. Figure 1(p) shows the $P_{\rm sat}$ of the two devices with different $V_{\rm DQ}$. In the figure, DCGC-HEMT shows a stronger power performance than DCTB-HEMT, especially at high $V_{\rm DQ}$. The effective electrostatic shielding effect contributes to the excellent large-signal characteristic of DCGC-HEMT.

Conclusion. The direct current and radio frequency of DCGC-HEMT and DCTB-HEMT were systematically investigated. Owing to the utilization of a graded-AlGaN bottom barrier to provide more carriers and shield traps in the buffer, DCGC-HEMT exhibited greater saturated drain current and suppression in drain lag, enabling it to show greater output performance than DCTB-HEMT. The improvement in the former's superior large-signal characteristic indicates its potential for high-performance RF PA applications.

Acknowledgements This work was supported by National Natural Science Foundation of China (Grant Nos. 62234009, 62090014, 62188102, 62104178, 62104179, 62104184), China Postdoctoral Science Foundation (Grant No. 2022T150505), Postdoctoral Fellowship Program of CPSF (Grant No. GZB20230557), Natural Science Basic Research Program of Shaanxi (Grant No. 2024JC-YBQN-0611), and Fundamental Research Funds for the Central Universities of China (Grant No. YJSJ23019).

Supporting information Appendix A. The supporting information is available online at info.scichina.com and link.springer.com. The supporting materials are published as submitted, without typesetting or editing. The responsibility for scientific accuracy and content remains entirely with the authors.

References

1 Desmaris V, Rudzinski M, Rorsman N, et al. Comparison of the DC and microwave performance of AlGaN/GaN HEMTs grown on SiC by MOCVD with Fe-doped or unintentionally doped GaN buffer layers. IEEE Trans Electron Dev, 2006, 53: 2413–2417

2 Bajaj S, Allerman A, Armstrong A, et al. High Al-content AlGaN transistor with 0.5 A/mm current density and lateral breakdown field exceeding 3.6 MV/cm. IEEE Electron Dev Lett, 2018, 39: 256–259

3 Zhu J, Jing S, Ma X, et al. Improvement of electron transport property and on-resistance in normally-OFF Al_2O_3/AlGaN/GaN MOS-HEMTs using post-etch surface treatment. IEEE Trans Electron Dev, 2020, 67: 3541–3547

4 Chu R, Zhou Y, Liu J, et al. AlGaN-GaN double-channel HEMTs. IEEE Trans Electron Dev, 2005, 52: 438–446

5 Ando Y, Ishikura K, Yamanoguchi K, et al. Theoretical and experimental study of inverse piezoelectric effect in AlGaN/GaN field-plated heterostructure field-effect transistors. IEEE Trans Electron Dev, 2012, 59: 3350–3356